Tracking the Cracking: a Holistic Analysis of Rapid Ice Shelf Fracture Using Seismology, Geodesy, and Satellite Imagery on the Pine Island Glacier Ice Shelf, West Antarctica

Seth Olinger[1,1], Bradley Paul Lipovsky[2,2,2], Marine Denolle[1,1,1], Brendan W Crowell[2,2,2], and Stephanie Olinger[1]

[1]Harvard University
[2]University of Washington

December 7, 2022

Abstract

Ice shelves regulate the stability of marine ice sheets. We track fractures on Pine Island Glacier , a quickly-accelerating glacier in West Antarctica that contributes more to sea level rise than any other glacier. Using an on-ice seismic network deployed from 2012 to 2014, we catalog icequakes that dominantly consist of flexural gravity waves. Icequakes occur near the rift tip and in two distinct areas of the shear margin, and TerraSAR-X imagery shows significant fracture in each source region. Rift-tip icequakes increase with ice speed, linking rift fracture to glaciological stresses and/or localized thinning. Using a simple flexural gravity wave model, we deconvolve wave propagation effects to estimate icequake source durations of 19.5 to 50.0 s, and transient loads of 3.8 to 14.0 kPa corresponding to 4.3 to 15.9 m of crevasse growth per icequake. These long source durations suggest that water flow may limit the rate of crevasse opening.

Posted on 7 Dec 2022 — CC-BY-NC 4 — https://doi.org/10.1002/essoar.10510107.3 — This a preprint and has not been peer reviewed. Data may be preliminary.

Tracking the Cracking: a Holistic Analysis of Rapid Ice Shelf Fracture Using Seismology, Geodesy, and Satellite Imagery on the Pine Island Glacier Ice Shelf, West Antarctica

S. D. Olinger[1,2], B. P. Lipovsky[2], M. A. Denolle[2], B. W. Crowell[2]

[1]Department of Earth and Planetary Sciences, Harvard University, Cambridge, Massachusetts, USA
[2]Department of Earth and Space Sciences, University of Washington, Seattle, Washington, USA

Key Points:

- Fracture at PIG generate flexural gravity waves, a wave type related to interaction between a floating plate and supporting fluid.
- Rift-tip seismicity rate increases with ice speed, either due to changes in the underlying ice shelf stress state or localized thinning.
- Recorded flexural gravity waves are consistent with a point load of ∼10 kPa applied over ∼30 s, corresponding to ∼10 m of vertical cracking.

Corresponding author: Stephanie D. Olinger, `stepholinger@fas.harvard.edu`

Abstract

Ice shelves regulate the stability of marine ice sheets. We track fractures on Pine Island Glacier, a quickly-accelerating glacier in West Antarctica that contributes more to sea level rise than any other glacier. Using an on-ice seismic network deployed from 2012 to 2014, we catalog icequakes that dominantly consist of flexural gravity waves. Icequakes occur near the rift tip and in two distinct areas of the shear margin, and TerraSAR-X imagery shows significant fracture in each source region. Rift-tip icequakes increase with ice speed, linking rift fracture to glaciological stresses and/or localized thinning. Using a simple flexural gravity wave model, we deconvolve wave propagation effects to estimate icequake source durations of 19.5 to 50.0 s, and transient loads of 3.8 to 14.0 kPa corresponding to 4.3 to 15.9 m of crevasse growth per icequake. These long source durations suggest that water flow may limit the rate of crevasse opening.

1 Plain Language Summary

Large shelves of floating ice strengthen glaciers in Antarctica, helping to protect against rapid sea level rise that can occur when glaciers flow into the ocean. Ice shelves can collapse through rapid cracking (synonym of fracturing), but it is difficult to directly observe cracking on ice shelves. In this paper, we track cracks on Pine Island Glacier, an ice shelf in Antarctica that is particularly vulnerable to collapse. We see cracks in pictures taken by satellites. Cracking causes the ice shelf to shake up and down, which we record using the same equipment that records earthquakes. We record shaking located at a set of cracks at the side of the ice shelf and at the tip of a single massive crack called a rift. Rift cracking seems related to the speed that the ice shelf is flowing. We also use a computer simulation of shaking to learn about the details of the crack process. Our simulation suggests that the crack process might be more complicated than a single crack opening evenly at a constant rate.

2 Introduction

Ice shelf fracture exerts a fundamental control on the stability of marine ice sheets and associated sea level fluctuations (Seroussi et al., 2020). In particular, understanding the past, present, and future stability of the West Antarctic Ice Sheet (WAIS) remains one of the great challenges of modern glaciological research and is itself closely related to ice shelf fracturing processes (Scambos et al., 2017). Fractures on ice shelves take on many forms including through-cutting rifts (Larour et al., 2004; Hulbe et al., 2010; Lipovsky, 2020), smaller-scale basal and surface crevasses (Rist et al., 2002; McGrath et al., 2012), hydraulic fracturing (Weertman, 1973; Banwell et al., 2013), and cliff failure (Clerc et al., 2019). Despite decades of progress, understanding of ice shelf fracture remains significantly hindered by a lack of direct observation (Benn et al., 2007). A number of basic questions remain or have only partially been addressed: What forces are involved in ice shelf fracture? Is ice shelf fracture a fast and brittle or slow and ductile process? To what degree is water involved in fracture propagation? Does ice shelf fracture growth happen at a constant rate or in bursts, and what controls its timing?

All of these questions can be addressed using seismology. Because seismic waves carry information about the dynamics of fracture, numerous previous studies have leveraged such signals, referred to as icequakes, for this purpose (Von der Osten-Woldenburg, 1990; Hammer et al., 2015; Chen et al., 2019; Winberry et al., 2020). Seismic studies on ice shelves have shown that crevasse propagation is intermittent (Bassis et al., 2007; Heeszel et al., 2014) and have highlighted environmental forcings that would be difficult to ascertain using only remotely sensed observations (Bassis et al., 2008; Olinger et al., 2019; Aster et al., 2021).

Here, we use seismic recordings to quantify fracturing of Pine Island Glacier (PIG) Ice Shelf. PIG, part of the larger WAIS, contributes more to present day global sea level rise than any other glacier (Shepherd et al., 2018). Current ice mass loss at PIG is thought to be due to the retreat of the floating ice shelf (Joughin, Shapero, Smith, et al., 2021) being caused by interactions between ocean forcing (Christianson et al., 2016; Joughin, Shapero, Dutrieux, & Smith, 2021) and fracturing processes (MacGregor et al., 2012).

We focus on icequakes that travel as flexural gravity waves to quantify fracturing of PIG Ice Shelf. Flexural gravity waves are a type of hybrid seismic-water wave (Ewing & Crary, 1934) unique to floating structures such as ice shelves since both elasticity and buoyancy act as their restoring force (Ewing & Crary, 1934). Flexural gravity waves are strongly dispersive (Ewing & Crary, 1934), which can make waveform analysis difficult and necessitates careful modelling (Sergienko, 2017; Mattsson et al., 2018; Lipovsky, 2018). Despite this challenge, flexural gravity waves are useful tools to study ice shelf processes because, while direct body waves in ice shelves are often not observed at distances greater than a few ice thickness (Zhan et al., 2014), flexural gravity waves are often observed to travel long distances from their exciting source (Williams & Robinson, 1981).

Many sources generate flexural gravity waves on ice shelves including ocean swell (Williams & Robinson, 1981), tsunamis (Bromirski et al., 2017), and airplane landings (MacAyeal et al., 2009). MacAyeal et al. (2009) appears to have been the first to propose that fracturing processes in ice shelves may act as seismic sources that generate flexural gravity waves. MacAyeal et al. (2009) considered water motion in a deforming rift and motion of detaching blocks from the ice front as two such sources. Here, we hypothesize that crevasse growth generates flexural gravity waves.

We begin our fracture analysis by describing a timeline of events with the use of satellite imagery. Next, we catalog flexural gravity waves on PIG to examine the relationship between crack growth, large-scale rift propagation, shear margin processes, and ice shelf acceleration. We then interrogate icequake source physics by modeling the ice shelf as a buoyantly supported beam, the simplest model that captures flexural gravity wave propagation (Sergienko, 2017; Mattsson et al., 2018). In our analysis, we model flexural gravity wave generation by a point load or bending moment applied during ice shelf crevasse growth to infer key source parameters of the recorded icequakes.

3 Analysis of Satellite Imagery and Positioning

We track visible fracturing on PIG using images collected by the TerraSAR-X satellite (Pitz & Miller, 2010) from 2012 to 2014. At the start of our study period in January 2012, the primary visible fractures are the rift, ∼20 large cracks extending into the ice shelf from northern shear margin, and ∼10 cracks extending into the ice shelf at the southern edge of the nascent iceberg (Figure 1a, left). By January 2013, the rift had propagated a few kilometers without significant widening, and two wing cracks (Renshaw & Schulson, 2001) opened at the rift tip (Figure 1a, right). One of the cracks at the northern shear margin extended 7 km and connected to the rift between May 8 and May 11, 2012. The other northern shear margin cracks extended and widened, at least two new cracks initiated near Evans Knoll, and one of cracks at the southern edge of the nascent iceberg extended to within a kilometer of the rift tip.

During the first four months of 2013, the wing cracks near the rift tip extended and widened. In early July 2013, a block of ice calved along a wing crack at the southern edge of the nascent iceberg near the rift tip (Figure 1b). After this preliminary calving event, the only connection between the nascent iceberg and the ice shelf was a 2 km wide strip of ice between the ocean and a wing crack. Over the next few months, we observe significant widening of the rift, likely due to the iceberg beginning to drift away from the ice shelf. Iceberg B-31 calved in November 2013 (Figure 1c) when left lateral motion of

the iceberg pried open a large wing crack near the rift tip until a strip of ice stabilizing the iceberg broke off, allowing Iceberg B-31 to drift into the sea. By the end of 2013, many fractures in the northern shear margin had extended and calved smaller icebergs, and several new fractures had initiated near Evans Knoll.

We examine Global Positioning System (GPS) speed timeseries derived from five continuous GPS stations. The GPS stations were co-located with seismometers (locations shown in Figure 2). Our GPS processing is described in Supporting Text S1. Figure 3a plots the GPS-derived ice shelf speed. We find that ice speed at PIG decreases from 11.1 m/day in January 2012 to 10.8 m/day in April 2013. Then, ice speed drops to below 10.6 m/day for eight days in early May 2013. Following this rapid slowdown, ice speed begins to increase, reaching 10.9 m/day by the end of 2013. The GPS ice speed we compute here is consistent with a previous study utilizing the same dataset (Christianson et al., 2016).

4 Analysis of Seismograms

We examine seismic data from five sites on PIG (Stanton et al., 2013). The instruments were deployed in January 2012 and retrieved in December 2013, providing two years of continuous data. The seismic stations were deployed in a cross shape with 5 km aperture at the center of the ice shelf (Figure 2). Each site consisted of a three component Nanometrics Trillium 120 Broadband seismometer and a Quanterra Q330 digitizer (David Holland & Robert Bindschadler, 2012). Seismic data was sampled at 100 Hz, and we removed the instrumental response on the frequency band 0.001 Hz to 45 Hz.

In the seismic dataset, we observe events with an abrupt onset and with high frequencies that arrive before low frequencies. This type of dispersion is characteristic of flexural gravity waves. The observed dispersion (high frequency waves travel faster) is the opposite of typical surface waves in the solid Earth. In the latter case, low frequency waves travel faster because seismic wave speeds generally increase with depth.

To detect flexural gravity waves in the dataset, we design a two-stage detection scheme that identifies broadband, dispersive seismic events. Our detection approach, detailed in Text S2, uses a dual-band short term average/long term average (STA/LTA) detector in combination with template matching (Allen, 1978; Gibbons & Ringdal, 2006) to detect a preliminary catalog of 22,119 events. Inspection of the preliminary catalog reveals two main families of events: one with clear high-frequency-first dispersion and one which is dominantly monochomatic. To isolate flexural gravity waves, we undertake waveform clustering using a K-Shape algorithm (Paparrizos & Gravano, 2016) modified to operate on multi-component seismic data. Visual analysis of the clustered catalog demonstrates the efficacy of our approach in isolating flexural gravity waves (Figure 3). Our final catalog contains 8,184 likely flexural gravity wave events, which we refer to as icequakes in the rest of the text.

We next determine locations for all icequakes in our final catalog. Given the poor distribution of the stations with respect to fracture locations, we employ single-station approaches to locating icequakes. We compute epicentral back-azimuths by analyzing the polarization direction of recorded horizontal waves (Aster et al., 2021). We apply principle component analysis (PCA) to the horizontal component seismograms to retrieve polarization directions. The polarization provides a 180 degree ambiguity, so we find the direction of propagation based on which station recorded the first arrival (see Text S3).

We locate all of the 8,184 icequakes to one of three distinct source regions: the rift tip, the body of the rift and nearby shear margin ("rift/margin"), and the northeast shear margin near Evan's knoll ("shear margin"), which are depicted in Figure 2. These spatial groups correspond to 22%, 29%, and 40% of the catalog, respectively, with 9% of events

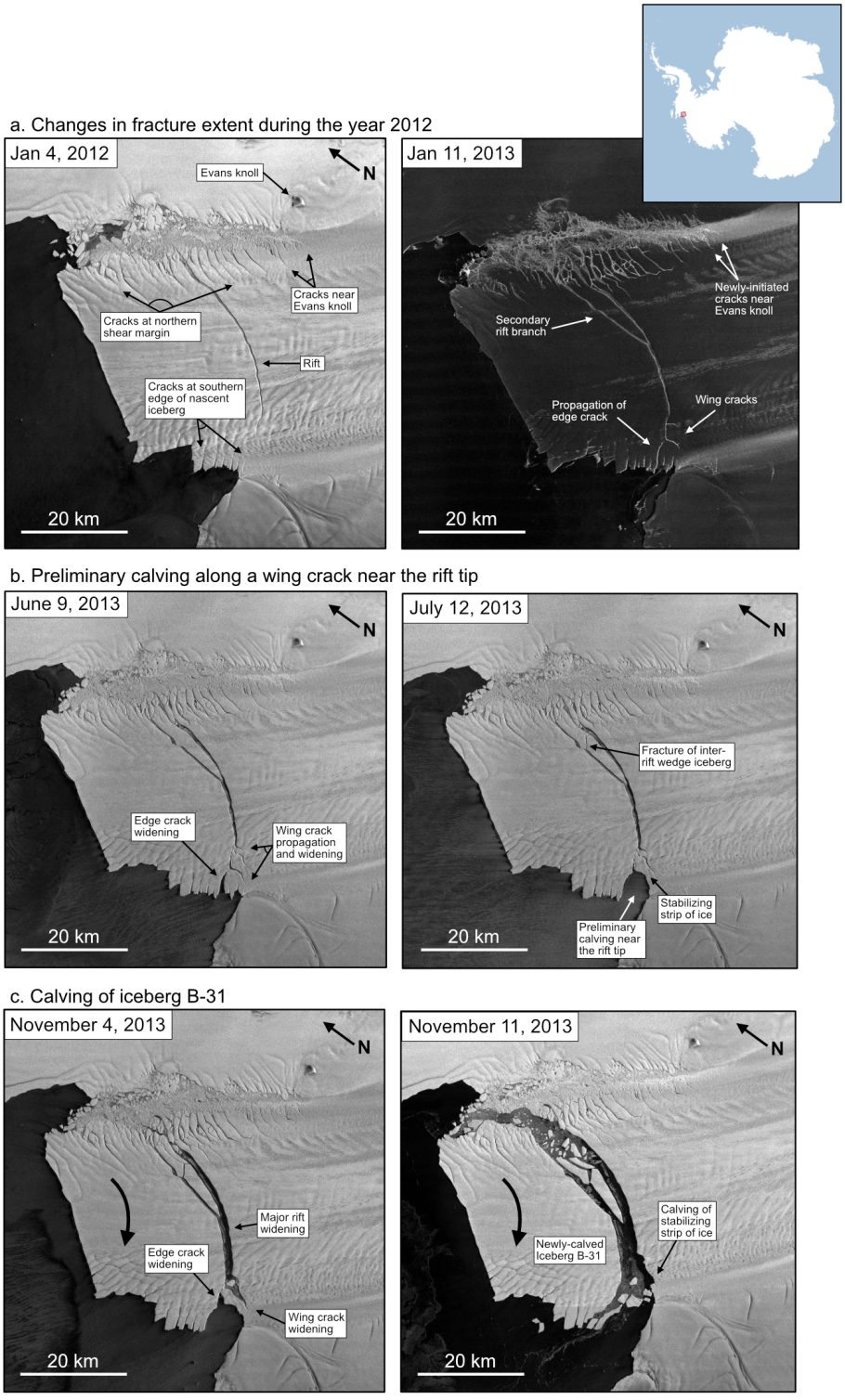

Figure 1. TerraSAR-X images showing an overview of fracture development at PIG from 2012 to 2014. Large arrow in panels c. and d. show sense of motion of the iceberg. See text for full discussion. Inset shows the location of PIG in Antarctica.

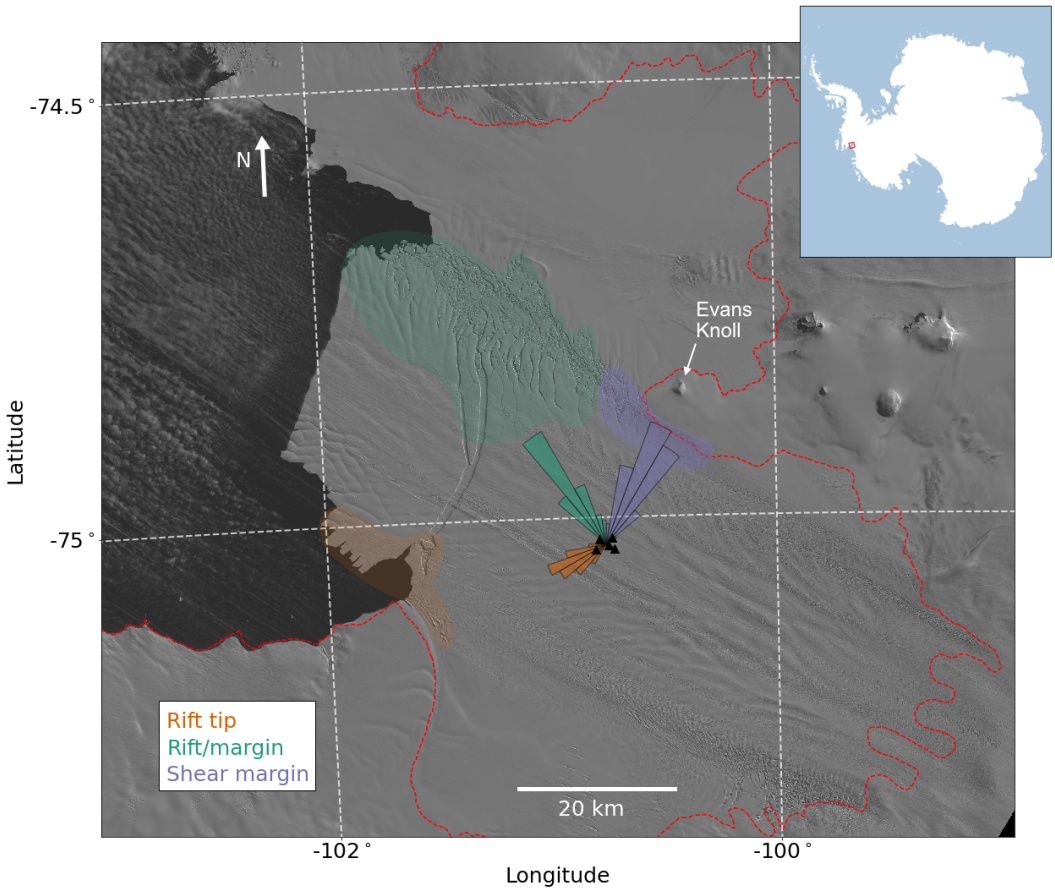

Figure 2. Back-azimuthal histogram showing locations of cataloged icequake. Rift-tip event back-azimuths are plotted as orange rays. Rift/margin event back-azimuths are plotted as green rays. Shear-margin event back-azimuths are plotted as purple rays. Likely source regions are shown by colored polygons. PIG array seismic and GPS stations are plotted as black triangles. Approximate grounding line position is shown by the red dashed line (Bindschadler et al., 2011). Background LANDSAT imagery is from October 2013 (courtesy of the United States Geological Survey).

having indeterminate locations. Figure 2 shows the back-azimuthal histograms of the three groups.

5 Relationships Between Icequakes and Ice Shelf Behavior

5.1 Rift tip

The rift-tip icequakes are coincident in space and time with several fracturing processes including rift propagation, wing cracking, small scale calving within the rift, and calving along the southern edge of the nascent iceberg. Rift tip events occurred more frequently in 2013 than in 2012 (Figure 3b). The mean seismicity rate was 9.4 icequakes/week in 2012 and 25.6 icequakes/week in 2013. 19 weeks of 2013 equaled or exceeded the maximum 2012 seismicity rate of 29 icequakes/week. Weekly icequake counts increased past the peak level seen in 2012 on May 21, 2013 and remain elevated until the end of the de-

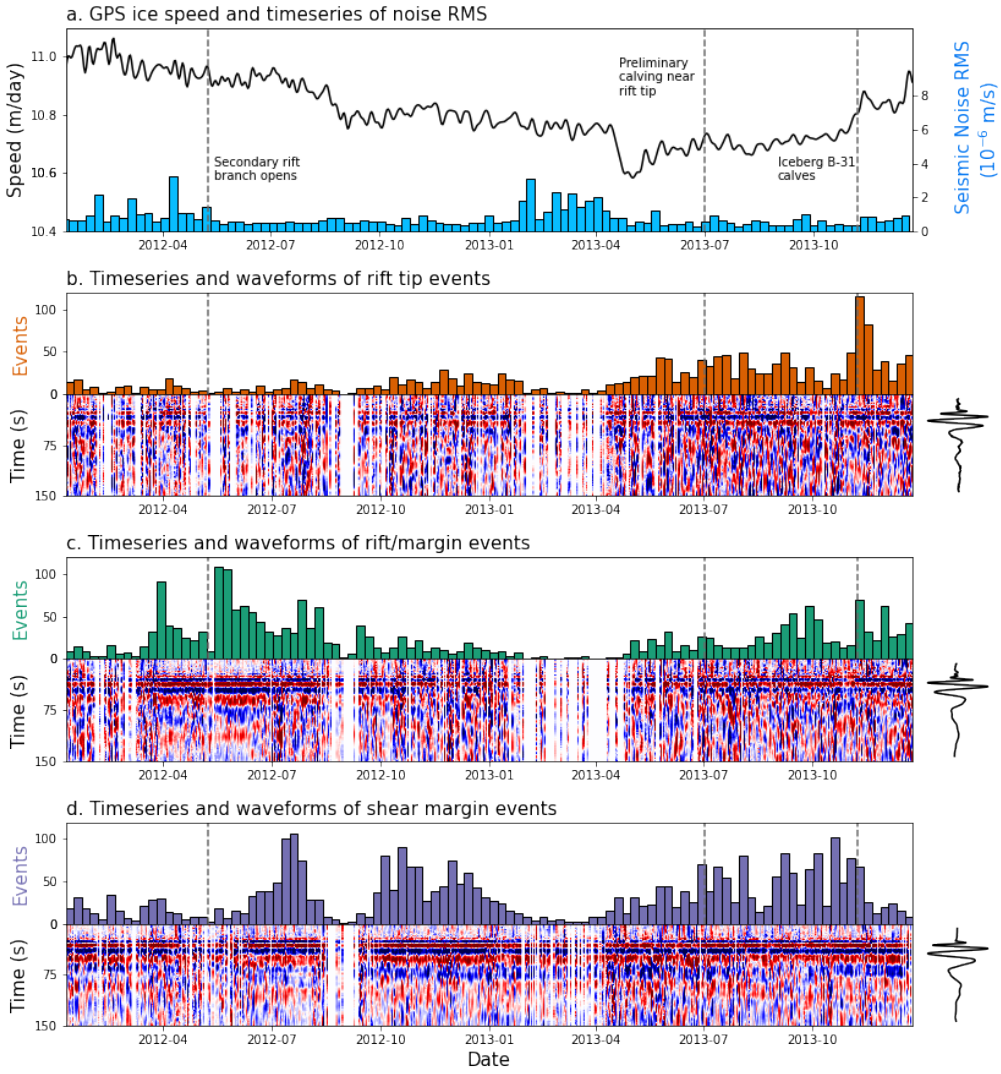

Figure 3. Timing and waveforms of cataloged icequake. (a) GPS-derived ice velocity is shown by the black line, and average seismic noise is shown by blue bars. Noise is highest in the Antarctic summer, when minimal sea ice is present to attenuate ocean-generated noise, reducing detectability in January, February, and March. (b) Rift-tip events. Weekly timeseries of rift tip event times is shown by orange bars. Daily vertical (HHZ) waveform stacks of detected rift tip events are plotted beneath. Overall rift-tip event stack is shown to the right. (c) Same as (b) for rift/margin events, color-coded in green. (d) Same as (b) for shear-margin events, color-coded in purple.

ployment. This period of elevated rift tip seismicity corresponds to the phase of significant wing crack growth and rift widening observed in imagery. Rift tip icequakes appear located ∼15 degrees south of the rift tip's position in LANDSAT imagery from October 12, 2013 (Figure 2). However, when Iceberg B-31 calved in November 2013, the wing crack extending south of the rift had propagated to a location consistent with the peak in the back-azimuthal distribution of rift tip icequakes (Figure 1c, left).

Peak levels of rift-tip seismicity were observed during the calving of Iceberg B-31 in the week of November 5, 2013. That week had 115 rift-tip events, the highest event count of any week across all three source regions. Furthermore, elevated rift-tip icequake activity in 2013 corresponds to a period of accelerating ice velocities (Figure 3a). While rift-tip fracture may be more directly related to strain rate in a viscous regime and strain in an elastic regime, we simply note that ice speed reflects the underlying stress state of the ice shelf. The correspondence in time between elevated rift-tip seismicity rates and increasing ice velocities therefore suggests that rift propagation is sensitive to the underlying stress state of the ice shelf. In addition, rift tip fracture may be enhanced by localized ice shelf thinning and melt within the rift. Christianson et al. (2016) hypothesize that the overall pattern of ice velocities at PIG in 2013 tracks a time-lagged response to ocean melting, and localized melt has been proposed as a primary driver of rifting at PIG (Walker & Gardner, 2019; Jeong et al., 2016). The observed connection in time between rift tip fracture and accelerated ice velocities demonstrates that rift growth and PIG is sensitive to changes in ice dynamics, localized melt, or a combination of both. At the present time, however, we are unable to confirm whether local or more distant melt-related feedbacks are responsible for the observed fracturing.

5.2 Rift/margin

The rift/margin icequakes are coincident in space and time with the growth of ∼20 rifts formed in the northwest shear zone, as well as smaller-scale fractures and widening of the main rift itself. Rift/margin icequakes occurred more frequently in 2012 than in 2013. The mean seismicity rate was 27.7 icequakes/week in 2012 and 19.3 icequakes/week in 2013. Four weeks of 2012 equaled or exceeded the maximum 2013 seismicity rate of 70 icequakes/week. The timing of icequakes in the rift/margin group is independent of ice speed. Peak levels of rift/margin seismicity were observed during the week of May 15, 2012, which contained 109 rift/margin icequakes. Rift/margin icequakes reach peak seismicity rates in the weeks following the opening of the secondary rift branch in May 2012, suggesting that the crack opening caused aftershock-like seismicity and/or destabilized the margin, enhancing the growth of nearby fractures.

5.3 Shear margin

The shear-margin icequakes are coincident in space and time with the initiation of new cracks and growth of extant cracks near Evans Knoll. This area marks the transition from a primarily intact shear margin upstream of Evans Knoll to a highly fractured shear margin downstream of Evans Knoll. Imagery shows that multiple fractures longer than 1 km were initiated in this area during 2012 and 2013 (Figure 1). Shear-margin icequakes occurred at an approximately equal rate in 2012 and 2013. The mean seismicity rate was 31.9 icequakes/week in 2012 and 32.2 icequakes/week in 2013. Peak levels of shear margin seismicity were observed during the week of July 17, 2012, which contained 107 shear-margin icequakes. Shear-margin icequakes do not exhibit any prominent temporal trends and appear independent of ice velocity. The shear margin experiences the highest overall level of seismic activity, suggesting that the transition point from intact to fractured ice near Evans Knoll experiences higher stress concentrations than either the rift tip or the rift/margin regions, consistent with rift modeling (Lipovsky, 2020).

6 Icequake Source Analysis

We next estimate the distribution of forces that gives rise to the observed seismograms. We do this by removing wave propagation effects from the observed seismograms using a numerically computed Green's function. Our catalog was designed to represent icequakes that mostly consist of flexural gravity waves. We therefore model the vertical seismograms using the simplest model that gives rise to flexural gravity waves, the dynamic floating beam equation (Ewing & Crary, 1934; Squire & Allan, 1977),

$$\rho_i h_i \frac{\partial^2 w}{\partial t^2} + D\frac{\partial^4 w}{\partial x^4} + \rho_w g w + \rho_w \frac{\partial \phi}{\partial t} = P, \tag{1}$$

where $D \equiv EI = Eh_i^3/[12(1-\nu^2)]$ is the flexural rigidity with second moment of area $I = \int_{-h_i/2}^{h_i/2} z^2 dz$, E is the Young's modulus of ice, ν is the Poisson's ratio of ice, t is time, x is horizontal position, g is gravitational acceleration constant, h_i is the ice thickness, ρ_i is the density of ice, ρ_w is the density of water, w is the vertical displacement of the beam, ϕ is the ocean surface velocity potential, and P is an applied point load. From left to right, the terms in Equation (1) represent inertia, flexure of the ice shelf, buoyancy, and ocean surface waves generated at the ice-water interface. We initially use a locally-averaged ice thickness of $h_i = 400$ m (Shean et al., 2019) and a water depth of $h_w = 590$ m (Fretwell et al., 2013).

We model icequake sources as either an applied point load or point bending moment. When a basal crevasse opens and fills with water, the downward-acting ice overburden stress at the top of the crevasse is greater in magnitude than the upward-acting buoyancy stress exerted by water filling the crevasse. This applies a downward point load to the ice shelf. In addition, the horizontal ice overburden stress along the walls of the crevasse is greater in magnitude than the horizontal buoyancy stress exerted by the water filling the crevasse. The difference in magnitude between these two stresses decreases with depth such that the walls of a crevasse are subject to stress gradient. This applies a bending moment to the ice shelf. These two mechanisms may act in concert and simultaneously apply a moment and point load to the ice shelf. We choose not to pursue such hybrid sources at the present time because the simplicity of our model –specifically the assumptions of uniform ice thickness and two-dimensional geometry– suggests that additional source complexity is not warranted prior to improvements in these other areas.

We obtain the Green's function of the floating beam equation as the impulse response of the mechanical system to a point load (force per unit length) source. Rewriting Equation 1 using the linear operator $\mathcal{A}$ as $\mathcal{A}w = P$, the Green's function equation can then be written as $\mathcal{A}G = \delta(x)\delta(t)$. In Supporting Text S4, we derive a frequency-wavenumber solution for G that we are able to analytically invert in the time domain and numerically invert in the frequency domain. We then derive G_m, the vertical displacement response to a point moment source.

We deconvolve G and G_m from waveform stacks to estimate the source load or moment distribution of events in each spatial group. Figure 4 shows our deconvolution result for the rift-tip icequakes, illustrating that a given vertical displacement seismogram may equivalently be represented as a point moment (Figure 4a and b) or a point load (Figure 4c and d). The equivalent analysis for the other two groups of events is given in Supporting Figures S1-2.

We examine the sensitivity of our deconvolution to the assumed value for the ice thickness by varying the ice thickness between 300 and 500 m (Figures S3-5). For the rift-tip group, we find source durations ranging from 30.48 to 50.00 s and amplitudes ranging from 2.69 to 6.90 MPa·m (point moment) and 3.83 to 8.62 kPa (point load). For the rift/margin group, we find source durations ranging from 19.52 to 48.57 s and amplitudes ranging from 3.82 to 12.55 MPa·m (point moment) and from 5.05 to 14.02 kPa (point

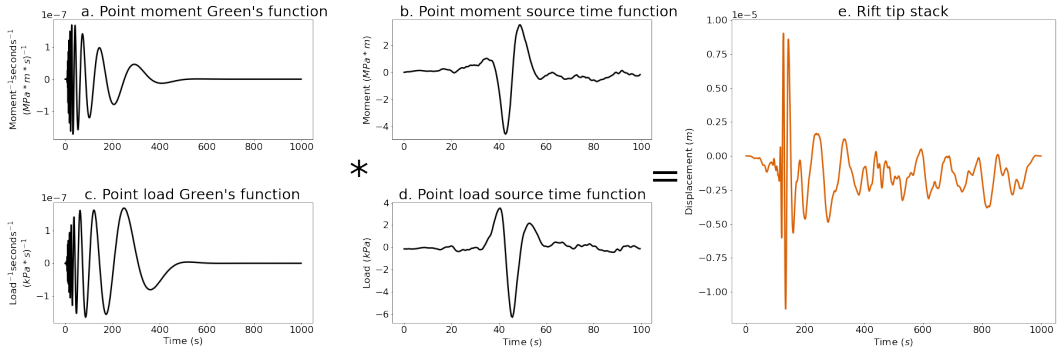

Figure 4. Green's functions and source time functions for rift tip events. (a) Theoretical Green's function for a point moment source located at a distance of 25 km, which is approximately the distance from PIG seismic array to the rift tip. (b) Source time function retrieved by deconvolving the point moment Green's function from the stack of rift tip vertical displacement waveforms. (c) Theoretical Green's function for a point load source located at a distance of 25 km. (d) Source time function retrieved by deconvolving the point load Green's function from the stack of rift tip vertical displacement waveforms. (e) Stack of rift tip vertical displacement waveforms obtained by aligning waveforms to a master event and taking the mean waveform on the frequency band 0.01-1 Hz.

load). Finally, for the shear-margin group, we find source durations ranging from 27.14 to 36.67 s and amplitudes ranging from 5.60 to 14.89 MPa·m (point moment) and from 8.04 to 12.97 kPa (point load).

7 Discussion of icequake source physics

How large were the cracks that generated the recorded flexural gravity waves? We estimate the amount of vertical crack opening for each spatial group using the point load source amplitudes (Text S5) for ice thickness varying between 300 and 500 m. Rift tip point load amplitudes correspond to 4.3 to 9.8 m of vertical crevasse opening. Rift/margin point load amplitudes correspond to 5.7 to 15.9 m of vertical crevasse opening. Shear-margin point load amplitudes correspond to 9.1 to 14.7 m of vertical crevasse opening. This suggests that the large-scale fracture opening and rift propagation observed in imagery (Figure 1) was the result of many discrete crack opening events that each spanned only about 1 % of the ice thickness, not the result of full-thickness crack opening. Bassis et al. (2007) and Heeszel et al. (2014) observed episodic rift seismicity on the Amery Ice Shelf and proposed that rifts might propagate due to the coalescence of smaller cracks. Our findings support the hypothesis that crack coalescence can act as a mechanism of rifting.

Estimated source time series for moment and point load exhibit one or several pulses of activity followed by a return to zero (Figure 4). Source time functions derived from body waves in an elastic medium result in estimates of moment rate (Aki & Richards, 2002, Equation 4.32). Here, however, our deconvolution is sensitive not to the rate of change of point load or moment, but instead to a point load and moment. This complicates the interpretation of the estimated source time series because it suggests that the icequakes represent the application and subsequent removal of some point load or moment. This physically counterintuitive situation motivates an examination of the sensitivity of our deconvolution to static offsets. We therefore calculate synthetic seismograms forced by a step in moment or point load (Figures S6-S8). We find that in some cases the step func-

tion provides an acceptable fit to the observations. We therefore are unable to infer whether the observed flexural gravity waves were generated by a pulse-like or step-like source.

The timescale of the source process, however, is constrained independent of the exact force distribution assumed in the deconvolution. Our source analysis implies that the recorded flexural gravity waves were generated by fracturing process with approximately 20-50 s duration. At this timescale, the observed waves must have been generated by brittle fracture, not by viscous deformation. This 20-50 s timescale is extremely slow compared, for example, to tectonic earthquakes, where earthquake duration scales like $10^{M/2}$ with earthquake moment M and 20 s duration is associated with a $M = 7$ earthquake (Ekström et al., 2003).

What process sets the duration of the observed icequakes? The above scaling for tectonic earthquakes is based on the reasoning that the duration is set by the time required for a shear crack to propagate across a fault of length L at a rate that tends towards inertial velocities (either the shear or dilatational wave speed v_s or v_p) (Freund, 1998). In our system, however, we expect that water plays a limiting role in the speed of fracture propagation that may not be present in tectonic earthquakes. The propagation of fluid filled basal crevasses is expected to occur at the crack wave speed (Lipovsky & Dunham, 2015). The crack wave speed is much slower than the inertial velocities and could plausibly be in the range of 1-100 m/s for basal crevasses in ice shelves. These velocities would suggest source length scales on the order of meters to hundreds of meters. A second plausible explanation is that long durations may be explained by the coalescence of many smaller individual fractures that open successively. And yet another explanation is that there could be significant horizontal propagation which is not captured in our model. We expect that more detailed near-source observations would be able to distinguish between these possible scenarios.

8 Conclusions

We detect and locate icequakes that propagate as flexural gravity waves on the Pine Island Glacier ice shelf from 2012 to 2014. When compared to satellite imagery, the back-azimuthal distribution of the detected events suggests that the icequakes were generated by fractures at the tip of a large rift and in two distinct portions of the northern shear margin. Most of the events were generated at the shear margin near Evans Knoll, in agreement with imagery that suggests significant fracture initiation. Increased fracturing at the rift tip is associated with increased ice speed and elevated basal melting in 2013 (Christianson et al., 2016). We attribute this relationship to changes in the stress state of the ice shelf or to melt-driven thinning that elevated rift tip stress concentrations. We use a simple model of flexural gravity waves to constrain the source of the recorded waves. We find that the observed waves have a source duration between 20-50 s. This timescale implies that a brittle fracture process generated the waves. Our analysis therefore confirms the role of brittle processes in the long-term evolution of marine ice sheets.

Acknowledgments

SDO and BPL were supported by the National Science Foundation (NSF) Office of Polar Programs (OPP) award #1853896. SDO was also supported by startup funds of MAD at Harvard University in the Department of Earth and Planetary Sciences. The facilities of IRIS Data Services and IRIS Data Management Center were used for access to waveforms, metadata, and/or derived products used in this study. IRIS Data Services are funded through the Seismological Facilities for the Advancement of Geoscience (SAGE) Award of the National Science Foundation under Cooperative Support Agreement EAR-1851048. The seismic and geodetic datasets were collected by David Holland and Robert Bindschadler (2012), and the seismic DOI is `https://doi.org/10.7914/sn/xc_2012`. Seismic instruments were

provided by the Incorporated Research Institutions for Seismology (IRIS) through the PASSCAL Instrument Center at New Mexico Tech. Data collected is available through the IRIS Data Management Center. The facilities of the IRIS Consortium are supported by the National Science Foundation's Seismological Facilities for the Advancement of Geoscience (SAGE) Award under Cooperative Support Agreement EAR-1851048. Geodetic data are based on services provided by the GAGE Facility, operated by UNAVCO, Inc., with support from the National Science Foundation and the National Aeronautics and Space Administration under NSF Cooperative Agreement EAR-1724794. GPS processing was done using the GipsyX software, licensed to BWC at University of Washington. TerraSAR-X images were obtained using the freely-available EOWEB GeoPortal courtesy of the German Aerospace Center (DLR). Code to reproduce the processing workflow for this paper is hosted at `https://zenodo.org/badge/latestdoi/468875023`.

References

Aki, K., & Richards, P. G. (2002). *Quantitative seismology*.

Allen, R. V. (1978, 10). Automatic earthquake recognition and timing from single traces. *Bulletin of the Seismological Society of America*, *68*(5), 1521-1532. Retrieved from `https://doi.org/10.1785/BSSA0680051521` doi: 10.1785/BSSA0680051521

Aster, R. C., Lipovsky, B. P., Cole, H. M., Bromirski, P. D., Gerstoft, P., Nyblade, A., ... Stephen, R. (2021). Swell-triggered seismicity at the near-front damage zone of the ross ice shelf. *Seismological Research Letters*.

Banwell, A. F., MacAyeal, D. R., & Sergienko, O. V. (2013). Breakup of the larsen b ice shelf triggered by chain reaction drainage of supraglacial lakes. *Geophysical Research Letters*, *40*(22), 5872–5876.

Bassis, J. N., Fricker, H. A., Coleman, R., Bock, Y., Behrens, J., Darnell, D., ... Minster, J.-B. (2007). Seismicity and deformation associated with ice-shelf rift propagation. *Journal of Glaciology*, *53*(183), 523–536. doi: 10.3189/002214307784409207

Bassis, J. N., Fricker, H. A., Coleman, R., & Minster, J.-B. (2008). An investigation into the forces that drive ice-shelf rift propagation on the amery ice shelf, east antarctica. *Journal of Glaciology*, *54*(184), 17–27. doi: 10.3189/002214308784409116

Benn, D. I., Warren, C. R., & Mottram, R. H. (2007). Calving processes and the dynamics of calving glaciers. *Earth-Science Reviews*, *82*(3-4), 143–179.

Bindschadler, R., Choi, H., Wichlacz, A., Bingham, R., Bohlander, J., Brunt, K., ... Young, N. (2011). Getting around antarctica: new high-resolution mappings of the grounded and freely-floating boundaries of the antarctic ice sheet created for the international polar year. *The Cryosphere*, *5*(3), 569–588. Retrieved from `https://tc.copernicus.org/articles/5/569/2011/` doi: 10.5194/tc-5-569-2011

Bromirski, P. D., Chen, Z., Stephen, R. A., Gerstoft, P., Arcas, D., Diez, A., ... Nyblade, A. (2017). Tsunami and infragravity waves impacting antarctic ice shelves. *Journal of Geophysical Research: Oceans*, *122*(7), 5786-5801. Retrieved from `https://agupubs.onlinelibrary.wiley.com/doi/abs/10.1002/2017JC012913` doi: https://doi.org/10.1002/2017JC012913

Chen, Z., Bromirski, P., Gerstoft, P., Stephen, R., Lee, W. S., Yun, S., ... Nyblade, A. (2019). Ross ice shelf icequakes associated with ocean gravity wave activity. *Geophysical Research Letters*, *46*(15), 8893–8902.

Christianson, K., Bushuk, M., Dutrieux, P., Parizek, B. R., Joughin, I. R., Alley, R. B., ... Holland, D. M. (2016). Sensitivity of pine island glacier to observed ocean forcing. *Geophysical Research Letters*, *43*(20), 10,817-10,825. Retrieved from `https://agupubs.onlinelibrary.wiley.com/doi/abs/`

10.1002/2016GL070500 doi: 10.1002/2016GL070500

Clerc, F., Minchew, B. M., & Behn, M. D. (2019). Marine ice cliff instability mitigated by slow removal of ice shelves. *Geophysical Research Letters*, *46*(21), 12108–12116.

David Holland, & Robert Bindschadler. (2012). *Observing pine island glacier (pig) ice shelf deformation and fracture using a gps and seismic network.* International Federation of Digital Seismograph Networks. Retrieved from https://www.fdsn.org/networks/detail/XC_2012/ doi: 10.7914/SN/XC_2012

Ekström, G., Nettles, M., & Abers, G. A. (2003). Glacial earthquakes. *Science*, *302*(5645), 622–624.

Ewing, M., & Crary, A. (1934). Propagation of elastic waves in ice. part ii. *Physics*, *5*(7), 181–184.

Fretwell, P., Pritchard, H. D., Vaughan, D. G., Bamber, J. L., Barrand, N. E., Bell, R., ... Zirizzotti, A. (2013). Bedmap2: improved ice bed, surface and thickness datasets for antarctica. *The Cryosphere*, *7*(1), 375–393. Retrieved from https://tc.copernicus.org/articles/7/375/2013/ doi: 10.5194/tc-7-375-2013

Freund, L. B. (1998). *Dynamic fracture mechanics.* Cambridge university press.

Gibbons, S. J., & Ringdal, F. (2006, 04). The detection of low magnitude seismic events using array-based waveform correlation. *Geophysical Journal International*, *165*(1), 149-166. Retrieved from https://doi.org/10.1111/j.1365-246X.2006.02865.x doi: 10.1111/j.1365-246X.2006.02865.x

Hammer, C., Ohrnberger, M., & Schlindwein, V. (2015). Pattern of cryospheric seismic events observed at ekström ice shelf, antarctica. *Geophysical Research Letters*, *42*(10), 3936–3943.

Heeszel, D. S., Fricker, H. A., Bassis, J. N., O'Neel, S., & Walter, F. (2014). Seismicity within a propagating ice shelf rift: The relationship between icequake locations and ice shelf structure. *Journal of Geophysical Research: Earth Surface*, *119*(4), 731-744. Retrieved from https://agupubs.onlinelibrary.wiley.com/doi/abs/10.1002/2013JF002849 doi: 10.1002/2013JF002849

Hulbe, C. L., LeDoux, C., & Cruikshank, K. (2010). Propagation of long fractures in the ronne ice shelf, antarctica, investigated using a numerical model of fracture propagation. *Journal of Glaciology*, *56*(197), 459–472. doi: 10.3189/002214310792447743

Jeong, S., Howat, I. M., & Bassis, J. N. (2016). Accelerated ice shelf rifting and retreat at pine island glacier, west antarctica. *Geophysical Research Letters*, *43*(22), 11,720-11,725. Retrieved from https://agupubs.onlinelibrary.wiley.com/doi/abs/10.1002/2016GL071360 doi: https://doi.org/10.1002/2016GL071360

Joughin, I., Shapero, D., Dutrieux, P., & Smith, B. (2021). Ocean-induced melt volume directly paces ice loss from pine island glacier. *Science advances*, *7*(43), eabi5738.

Joughin, I., Shapero, D., Smith, B., Dutrieux, P., & Barham, M. (2021). Ice-shelf retreat drives recent pine island glacier speedup. *Science Advances*, *7*(24), eabg3080.

Larour, E., Rignot, E., & Aubry, D. (2004). Modelling of rift propagation on ronne ice shelf, antarctica, and sensitivity to climate change. *Geophysical research letters*, *31*(16).

Lipovsky, B. P. (2018). Ice shelf rift propagation and the mechanics of wave-induced fracture. *Journal of Geophysical Research: Oceans*, *123*(6), 4014-4033. doi: https://doi.org/10.1029/2017JC013664

Lipovsky, B. P. (2020). Ice shelf rift propagation: stability, three-dimensional effects, and the role of marginal weakening. *The Cryosphere*, *14*(5), 1673–1683. doi: 10.5194/tc-14-1673-2020

Lipovsky, B. P., & Dunham, E. M. (2015). Vibrational modes of hydraulic fractures:

Inference of fracture geometry from resonant frequencies and attenuation. *Journal of Geophysical Research: Solid Earth*, *120*(2), 1080–1107.

MacAyeal, D. R., Okal, E. A., Aster, R. C., & Bassis, J. N. (2009). Seismic observations of glaciogenic ocean waves (micro-tsunamis) on icebergs and ice shelves. *Journal of Glaciology*, *55*(190), 193–206.

MacGregor, J. A., Catania, G. A., Markowski, M. S., & Andrews, A. G. (2012). Widespread rifting and retreat of ice-shelf margins in the eastern amundsen sea embayment between 1972 and 2011. *Journal of Glaciology*, *58*(209), 458–466.

Mattsson, K., Dunham, E. M., & Werpers, J. (2018). Simulation of acoustic and flexural-gravity waves in ice-covered oceans. *Journal of Computational Physics*, *373*, 230–252.

McGrath, D., Steffen, K., Scambos, T., Rajaram, H., Casassa, G., & Lagos, J. L. R. (2012). Basal crevasses and associated surface crevassing on the larsen c ice shelf, antarctica, and their role in ice-shelf instability. *Annals of glaciology*, *53*(60), 10–18.

Olinger, S. D., Lipovsky, B. P., Wiens, D. A., Aster, R. C., Bromirski, P. D., Chen, Z., ... Stephen, R. A. (2019). Tidal and thermal stresses drive seismicity along a major ross ice shelf rift. *Geophysical Research Letters*, *46*(12), 6644-6652. Retrieved from `https://agupubs.onlinelibrary.wiley.com/doi/abs/10.1029/2019GL082842` doi: 10.1029/2019GL082842

Paparrizos, J., & Gravano, L. (2016, June). K-shape: Efficient and accurate clustering of time series. *SIGMOD Rec.*, *45*(1), 69–76. Retrieved from `https://doi.org/10.1145/2949741.2949758` doi: 10.1145/2949741.2949758

Pitz, W., & Miller, D. (2010). The terrasar-x satellite. *IEEE Transactions on Geoscience and Remote Sensing*, *48*(2), 615-622. doi: 10.1109/TGRS.2009.2037432

Renshaw, C. E., & Schulson, E. M. (2001). Universal behaviour in compressive failure of brittle materials. *Nature*, *412*(6850), 897–900.

Rist, M., Sammonds, P., Oerter, H., & Doake, C. (2002). Fracture of antarctic shelf ice. *Journal of Geophysical Research: Solid Earth*, *107*(B1), ECV–2.

Scambos, T. A., Bell, R. E., Alley, R. B., Anandakrishnan, S., Bromwich, D., Brunt, K., ... others (2017). How much, how fast?: A science review and outlook for research on the instability of antarctica's thwaites glacier in the 21st century. *Global and Planetary Change*, *153*, 16–34.

Sergienko, O. (2017, 07). Behavior of flexural gravity waves on ice shelves: Application to the ross ice shelf. *Journal of Geophysical Research: Oceans*, *122*. doi: 10.1002/2017JC012947

Seroussi, H., Nowicki, S., Payne, A. J., Goelzer, H., Lipscomb, W. H., Abe-Ouchi, A., ... others (2020). Ismip6 antarctica: a multi-model ensemble of the antarctic ice sheet evolution over the 21st century. *The Cryosphere*, *14*(9), 3033–3070.

Shean, D. E., Joughin, I. R., Dutrieux, P., Smith, B. E., & Berthier, E. (2019). Ice shelf basal melt rates from a high-resolution digital elevation model (dem) record for pine island glacier, antarctica. *The Cryosphere*, *13*(10), 2633–2656. Retrieved from `https://tc.copernicus.org/articles/13/2633/2019/` doi: 10.5194/tc-13-2633-2019

Shepherd, A., Ivins, E., Rignot, E., Smith, B., Van Den Broeke, M., Velicogna, I., ... others (2018). Mass balance of the antarctic ice sheet from 1992 to 2017. *Nature*, *558*, 219–222.

Squire, V. A., & Allan, A. (1977). *Propagation of flexural gravity waves in sea ice*. Centre for Cold Ocean Resources Engineering, Memorial University of Newfoundland.

Stanton, T. P., Shaw, W., Truffer, M., Corr, H., Peters, L., Riverman, K., ... Anandakrishnan, S. (2013). Channelized ice melting in the ocean boundary layer beneath pine island glacier, antarctica. *Science*, *341*(6151), 1236–1239.

Von der Osten-Woldenburg, H. (1990). Icequakes on ekström ice shelf near atka bay, antarctica. *Journal of Glaciology*, *36*(122), 31–36.

Walker, C., & Gardner, A. (2019). Evolution of ice shelf rifts: Implications for formation mechanics and morphological controls. *Earth and Planetary Science Letters*, *526*, 115764. Retrieved from `https://www.sciencedirect.com/science/article/pii/S0012821X1930456X` doi: https://doi.org/10.1016/j.epsl.2019.115764

Weertman, J. (1973). Can a water-filled crevasse reach the bottom surface of a glacier. *IASH publ*, *95*, 139–145.

Williams, R., & Robinson, E. (1981). Flexural waves in the ross ice shelf. *Journal of Geophysical Research: Oceans*, *86*(C7), 6643–6648.

Winberry, J. P., Huerta, A. D., Anandakrishnan, S., Aster, R. C., Nyblade, A. A., & Wiens, D. A. (2020). Glacial earthquakes and precursory seismicity associated with thwaites glacier calving. *Geophysical Research Letters*, *47*(3), e2019GL086178. Retrieved from `https://agupubs.onlinelibrary.wiley.com/doi/abs/10.1029/2019GL086178` (e2019GL086178 2019GL086178) doi: 10.1029/2019GL086178

Zhan, Z., Tsai, V. C., Jackson, J. M., & Helmberger, D. (2014). Ambient noise correlation on the amery ice shelf, east antarctica. *Geophysical Journal International*, *196*(3), 1796–1802.

Supporting Information for "Tracking the Cracking: a Holistic Analysis of Rapid Ice Shelf Fracture Using Seismology, Geodesy, and Satellite Imagery on the Pine Island Glacier Ice Shelf, West Antarctica"

S. D. Olinger[1,2], B. Lipovsky[2], M. Denolle[2], B. Crowell[2]

[1]Department of Earth and Planetary Sciences, Harvard University, Cambridge, Massachusetts, USA

[2]Department of Earth and Space Sciences, University of Washington, Seattle, Washington, USA

Contents of this file

1. Text S1, GPS Processing

We processed five continuous GPS stations in the region, BOAR and SOW1-4 from 2012 to 2014. Each station was positioned kinematically in the International Terrestrial Reference Frame (ITRF) at a 30 s sample rate with GipsyX, using final Jet Propulsion Laboratory orbits. Ocean tidal loading and solid Earth tides were not removed from the derived displacement time series as these terms are needed to obtain the full glacial

dynamics. After obtaining the 30 s ITRF solutions, we performed a 5 min weighted average using the inverse of the individual epoch uncertainties for data weights, and then rotated the XYZ displacements into local North, East, and up displacements.

We obtain ice speed from the processed GPS positions at the GPS station SOW3 by calculating the total distance moved in each day of the deployment and differentiating with respect to time. The resulting ice speed curve contains some spike artifacts that arise from numerical differentiation, which we remove by linearly interpolating between the ice speed before and after the affected time period. Finally, we low pass filter the data to remove trends on time periods shorter than a week.

2. Text S2, Seismogram analysis

2.1. Icequake detection

To detect flexural gravity icequakes in the dataset, we design a two-stage detection scheme that identifies broadband, dispersive seismic events. First, we employ a short term average/long term average (STA/LTA) impulsivity detector. This method identifies high-amplitude impulsive events by comparing the mean amplitude of a short time window with the mean amplitude of a long time window (Allen, 1978). The detector is triggered when STA exceeds LTA by some threshold. STA/LTA threshold values are selected by tuning the algorithm to successfully detect high signal-to-noise ratio manually-identified events (see Table S1). We carry out STA/LTA on the vertical component of each station separately in two different frequency bands (0.01-1 Hz and 1-10 Hz). Selected waveforms satisfy the STA/LTA trigger criteria in both frequency bands on at least three out of the five stations. We refine the catalog and generate waveform templates by cross-correlating

each preliminary event with a master event waveform and selecting the events with cross correlation coefficients exceeding 0.9. This selection procedure resulted in 57 template events.

Second, we perform a template matching technique based on cross-correlation to identify events that were similar to the events in the preliminary catalog (Gibbons & Ringdal, 2006). To detect new events, each template event is cross correlated with all time windows in the dataset on two frequency bands (0.05-1 Hz and 1-10 Hz). We increase the lower frequency bound from 0.01 Hz to 0.05 Hz since many template events contained uninterpretable noise at frequencies below 0.05 Hz. The detector is triggered when the cross-correlation coefficient between a template event waveform and the given time window exceeds a threshold. The threshold value is selected so that the algorithm successfully detects the other known events of the preliminary catalog (see Supporting Table S1). Detected waveforms satisfy the trigger criteria on at least three out of the five stations in both frequency bands. We carry out this procedure for each template and removed redundant detections to yield the final catalog.

We detect 22,119 seismic events using the two-band template matching scheme. The detected events have a typical duration of around 50 s and an average peak vertical velocity of approximately $1 \cdot 10^{-5}$ m/s. Event waveforms vary in shape, indicating varied sources and propagation paths. Many of the events exhibit characteristic dispersion between 0.05 and 1 Hz with high frequencies arriving before low frequencies, while others were monochromatic between 0.05 and 1 Hz.

2.2. Waveform Clustering

Because the catalog of detected events contains both dispersive and monochromatic waveforms, we seek to cluster the events into groups based on wave shape. To do so, we modify the K-shape algorithm of Paparrizos and Gravano (2016). K-shape is designed specifically to cluster time series data. Instead of calculating the Euclidean distance between potential cluster centers and observations, K-shape calculates distances using the maximum normalized cross correlation coefficient between two time series. We adapt the K-shape algorithm for three component seismic data by independently computing the cross-correlation time series between the three separate seismic channels (vertical, East, and North). We then sum these three cross-correlation time series and calculate the distance metric as the maximum value of this summed cross correlation time series.

We use the K-shape algorithm to divide the catalog into $2, 3, \cdots, 20$ clusters. However, beyond two clusters, the differences between waveforms in each cluster become progressively less clear, and an analysis of the average distance from waveforms to their cluster center does not show significant improvement for larger numbers of clusters. We thus use the K-shape algorithm to divide the catalog into two distinct clusters, which differ based on waveform dispersion. The first cluster contains 8,184 dispersive events. The second cluster contains 13,935 monochromatic events that do not exhibit dispersion within the chosen frequency band. This difference suggests that the two types of waveforms may have been generated by different source processes. Since we are specifically interested in dispersive flexural gravity wave signals, we restrict the remaining analysis to the dispersive cluster.

3. Text S3. Methods for computing event back-azimuths.

3.1. Robust first arrival determination

We obtain the relative first arrival time of each event through phase lags measurements. We cross-correlate each respective component waveform between each seismic station. We choose a window length of 500 s around the first arrival. The trace that requires the largest shift forward in time to align with the other traces is taken to be the station of first arrival. In most cases, the first arrivals obtained independently using each component are in agreement for at least two components out of three. However, if all three components produce different stations of first arrival, a back-azimuth is not calculated and the event is disregarded.

3.2. Amplitude threshold

Next, we ensure that the polarization is extracted over a high signal to noise ratio event as against noise. We slide through the event waveform in 10 s windows with a step size of five seconds. For each 10 s time window, we check if the average amplitude of that window exceeds the average amplitude of the entire 500 s event window.

3.3. Principal component analysis

For time windows with sufficiently large amplitude, principal component analysis (PCA) is performed on the HHE (East) and HHN (North) traces from each station to retrieve the PCA components. The PCA first component is a vector whose direction explains the largest contribution of the data variance. It is equivalent to the eigenvector of the data covariance matrix that has the largest eigenvalue.

3.4. PCA first component vector correction

For waves polarized in the direction of propagation, the PCA first component vector corresponds to one of the two possible propagation directions separated by 180 degrees. Using the PCA first component vector and the geometry of the array, we compute the predicted stations of first arrival corresponding to both possible propagation directions. If the station of first arrival is in the direction of the PCA back-azimuth, the PCA first component's sign is preserved. If the station of first arrival is in the opposite direction (PCA azimuth+180 degree), we add 180 degrees to the PCA first component azimuth. This ensures that the PCA first component vector points in the direction from which incoming waves arrived.

3.5. Determining the predicted first arrival

We try three methods of computing the predicted station of first arrival corresponding to both possible propagation directions.

In the first method, we compare both possible phase back-azimuths to the back-azimuths of each station with respect to the mean station location, or array centroid. The stations that are radially closest to each possible back-azimuth are predicted to be the two possible first arrivals. The sign of the PCA first component vector is then adjusted to match the propagation direction whose predicted first arrival agree with the observed first arrival. Phases for which neither predicted first arrival agreed with the observed first arrival are discarded.

In the second method, we divide the array into two sectors along a line through the array centroid orthogonal to the PCA first component vector. The sign of the PCA first

component vector is then adjusted to match the propagation direction corresponding to the sector containing the observed first arrival. No phases are discarded.

In the third method, we compute the distance vector from the array centroid to each station. For incoming plane waves, the station farthest from the array centroid in the direction of propagation records the first arrival. The stations whose distance vectors have the largest component oriented in each possible propagation directions are predicted to be the two possible first arrivals. The sign of the PCA first component vector is then adjusted to match the propagation direction whose predicted first arrival agree with the observed first arrival. Phases for which neither predicted first arrival agreed with the observed first arrival are discarded. All three methods gave relatively consistent results.

3.6. Back-azimuth stacking

Next, we sum the PCA first component vectors across each station to obtain an average vector whose norm indicates the level of agreement between propagation directions calculated at each station. Finally, we take the arctangent of the quotient of the two elements of the PCA component vector to retrieve a back-azimuth. Because this procedure is repeated for each 10 s time window in the event, the result for each individual event is a distribution of back-azimuths calculated for each time window within that event.

To obtain a single back-azimuth for each event, we take the average of the back-azimuths calculated using each time window in the data. We use the mean of circular quantities, with the back-azimuth from each time window weighted by the norm of the summed PCA components across the array for that window. This means that time windows with poor agreement between stations are downweighted when taking the average back-azimuth. The

weighted mean of circular quantities is expressed below for the back-azimuth distribution $\theta_1, ..., \theta_n$ with PCA norms $w_1, ..., w_n$ of a single event with n time windows:

$$\bar{\theta} = \text{atan2}\left(\frac{1}{n}\sum_{j=1}^{n} w_j \sin(\theta_j), \frac{1}{n}\sum_{j=1}^{n} w_j \cos(\theta_j)\right) \tag{1}$$

3.7. Uncertainties in icequake back-azimuths

Uncertainties for icequake back-azimuths were computed using the weighted standard deviation of circular quantities for each event. The weighted standard deviation of circular quantities is expressed below for the back-azimuth distribution $\theta_1, ..., \theta_n$ with PCA norms $w_1, ..., w_n$ of a single event with n time windows:

$$\sigma = \sqrt{\left(\frac{1}{n}\sum_{j=1}^{n} w_j \sin(\theta_j)\right)^2 + \left(\frac{1}{n}\sum_{j=1}^{n} w_j \cos(\theta_j)\right)^2} \tag{2}$$

The mean back-azimuthal uncertainty for rift-tip icequakes was 26.16°. The mean back-azimuthal uncertainty for rift/margin icequakes was 17.26°. The mean back-azimuthal uncertainty for shear margin icequakes was 20.13°.

The slight mislocation of the rift-tip icequake back-azimuths apparent in Figure 2 is explained in a few ways. First, imagery suggests that much of the rift-tip fracture in 2013 occurred at the large wing extending south of the rift axis. The distribution of rift-tip seismic event back-azimuths points just south of this crack by $\sim 1°$. We note that the LANDSAT image displayed in Figure 2 is from October 12, 2013, about a month before the large swarm of rift-tip seismicity in November 2013. Because the wing crack continued to advance and widen in the month after the LANDSAT image was captured, we expect fracturing and seismicity to have occurred in front of the wing crack tip's

position in Figure 2. Second, the correspondence in time between the large swarm of rift-tip icequakes in November 2013 and visible fracture evolution at the rift-tip wing crack suggests that the recorded icequakes were generated by that fracture. Third, seismicity in front of a rift's visible extent was observed at the Amery Ice Shelf by Bassis et al. (2007) and may indicate that the wing crack was more advanced at depth than at the surface, explaining events whose back-azimuths point just in front of the crack. Finally, no other areas consistent with distribution of rift-tip icequake back-azimuths contain any visible fracture opening or growth, suggesting that the large amount of fracture evolution at the rift tip observed in imagery is the most likely source of the recorded icequakes.

4. Text S4, Flexural gravity wave model

4.1. Analytical Solution for Ocean Surface Waves

We examine the water velocity potential function ϕ and relate it to the vertical ice shelf velocity w. We first solve the ocean surface wave equation for a body of water with infinite length and finite depth:

$$\frac{\partial^2 \phi}{\partial x^2} + \frac{\partial^2 \phi}{\partial y^2} = 0 \tag{3}$$

over the interval $-\infty < x < \infty, -h_w < y < 0$. We enforce zero velocity at the ocean floor and couple vertical velocity to the rate of beam deflection at the ocean surface:

$$\frac{\partial \phi}{\partial y}\Big|_{y=-h_w} = 0 \qquad \frac{\partial \phi}{\partial y}\Big|_{y=0} = \frac{\partial w}{\partial t} \tag{4}$$

We enforce the Sommerfeld radiation condition:

$$\begin{aligned} \phi\big|_{x\to-\infty} = \frac{\partial \phi}{\partial x}\big|_{x\to-\infty} = 0 \\ \phi\big|_{x\to\infty} = \frac{\partial \phi}{\partial x}\big|_{x\to\infty} = 0 \end{aligned} \tag{5}$$

We employ the Fourier Transform, written for an arbitrary function $f(x)$ as

$$\bar{f}(k) = \int_{-\infty}^{\infty} f(x) e^{-i\xi x} dx$$

Applying the Fourier Transform in x to each term of Equation 3 yields:

$$\int_{-\infty}^{\infty} \frac{\partial^2 \phi}{\partial x^2} e^{-i\xi x} dx + \frac{\partial^2 \bar{\phi}}{\partial y^2} = 0$$

Evaluating the integral term:

$$e^{-i\xi x} \frac{\partial \phi}{\partial x}\Big|_{-\infty}^{\infty} + i\xi e^{-i\xi x} \phi\Big|_{-\infty}^{\infty} - \xi^2 \bar{\phi} \; + \frac{\partial^2 \bar{\phi}}{\partial y^2} = 0$$

We then apply the radiation condition (Equation 5) to eliminate the first two terms, resulting in an ordinary differential equation of $\bar{\phi}$:

$$-\xi^2 \bar{\phi} \; + \frac{\partial^2 \bar{\phi}}{\partial y^2} = 0 \tag{6}$$

By applying the vertical boundary conditions (Equation 4), we obtain the time-wavenumber domain solution that satisfies the governing equation and boundary conditions:

$$\bar{\phi} = \frac{\partial \bar{w}}{\partial t} \left(\frac{\cosh(\xi(h_w + y))}{\xi \sinh(h_w \xi)} \right) \tag{7}$$

We note that ϕ is a linear function of w, therefore permitting us to write the floating beam equation using the linear operator $\mathcal{A}$ as noted in the main text.

4.2. Analytic Solution for Buoyant Ice Shelf Flexure

To interrogate the source process that explains the observations, we obtain the Green's function, or fundamental solution of a floating dynamic beam to an impulse forcing. We

obtained the Green's function by using integral transform methods to solve the governing equation for an impulse forcing in space and time. We write the Green's function formulation of Equation 1 from the main text:

$$\rho_i h_i \frac{\partial^2 G}{\partial t^2} + D\frac{\partial^4 G}{\partial x^4} + \rho_w g G + \rho_w \frac{\partial \phi}{\partial t} = \delta(x)\delta(t) \tag{8}$$

where G is the Green's function, $\delta(x)$ is Dirac delta function in space, and $\delta(t)$ is the Dirac delta function in time. As before, we apply the Fourier Transform in space to each term. Next, we apply the Laplace transform, defined as,

$$g^*(s) = \int_0^\infty g(t)e^{-st}dt$$

Applying both the Fourier and Laplace Transforms to Equation 8 yields:

$$\rho_i h_i s^2 \bar{G}^* + D\xi^4 \bar{G}^* + \rho_w g \bar{G}^* + \rho_w \gamma s^2 \bar{G}^* = 1$$

We can then solve for $\bar{G}^*$ algebraically:

$$\bar{G}^* = \frac{\frac{1}{\rho_i h_i + \rho_w \gamma}}{\frac{D\xi^4 + \rho_w g}{\rho_i h_i + \rho_w \gamma} + s^2} \tag{9}$$

Finally, we analytically compute the inverse Laplace transform of Equation 9 to obtain the Fourier-transformed Green's function,

$$\bar{G}(k,t) = \frac{\sin\left(t\sqrt{\frac{D\xi^4 + \rho_w g}{\rho_i h_i + \rho_w \gamma}}\right)}{\sqrt{\rho_i h_i + \rho_w \gamma}\sqrt{D\xi^4 + \rho_w g}} \tag{10}$$

In practice, we numerically calculate $\bar{G}$ for a range of times and wavenumbers that define the temporal and spatial domain of the model run. Once $\bar{G}$ is calculated for each element of a vector of times and a vector of wavenumbers, the IFFT (inverse fast Fourier

transform) is taken to numerically retrieve the Green's function $G(x,t)$ of the ice shelf for an applied unit point force.

4.3. Greens function for a point moment source

To retrieve the impulse response to a point bending moment source, we note that an applied bending moment is equivalent to a pair of infinitesimally-spaced point loads with opposite signs:

$$G_m(x,t) = [G(x,t) - G(x+\Delta x,t)]_{\Delta x \to 0}$$
$$G(x,t) = \Delta x \left[\frac{G(x,t) - G(x+\Delta x,t)}{\Delta x}\right]_{\Delta x \to 0}$$
$$G(x,t) = \frac{dG(x,t)}{dx}$$

To obtain $G_m(x,t)$, we numerically take the spatial derivative of the point load Green's function $G(x,t)$.

4.4. Deconvolution procedure

We calculate source load through the deconvolution,

$$P_{\text{estimated}}(t) = \mathcal{F}^{-1}\left[\frac{\hat{w}(\omega)_{\text{observed}}}{\hat{G}(x_0,\omega)}\right], \tag{11}$$

where hats denote Fourier-transformed quantities, $\mathcal{F}^{-1}$ is the inverse Fourier transform, $w_{\text{observed}}(t)$ is a linear stack of observed displacement seismograms, $P_{\text{estimated}}(t)$ is an estimated source load distribution, and x_0 is the station epicentral distance. We obtain $w_{\text{observed}}(t)$ for each spatial group by aligning each waveform in the group with respect to a master event using cross correlation and taking the average waveform. Master events were selecting by finding the event from each spatial group that was best-correlated with

the overall centroid of the dispersive cluster. We choose x_0 corresponding to the average distance to each spatial group: for the rift tip, $x_0 = 25$ km; for rift/margin, $x_0 = 25$ km; for margin icequakes, $x_0 = 17.5$ km. We alternatively consider a bending moment source through the relationship,

$$M_{\text{estimated}}(t) = \mathcal{F}^{-1}\left[\frac{w(\omega)_{\text{observed}}}{G_m(x_0,\omega)}\right]. \tag{12}$$

5. Text S5, Estimating vertical crack extent from point load magnitude

The point load applied during vertical crack growth arises from the difference in ice overburden stress above the crack and buoyancy stress exerted by the water that fills the crack. Therefore, we write the following expression and substitute in the each stress:

$$\begin{aligned} P &= \sigma_{\text{overburden}} - \sigma_{\text{buoyancy}} \\ P &= \rho_i g(h_i - \Delta z_c) - \rho_w g(z_w - \Delta z_c) \end{aligned} \tag{13}$$

where P is the applied point load, ρ_i is the density of ice, ρ_w is the density of water, h_i is the ice shelf thickness, Δz_c is the change in vertical position of the crack tip, and z_w is the position of the water line.

Substituting the expression for the water line position $z_w = \frac{\rho_i}{\rho_w} h_i$ and simplifying gives:

$$P = g\Delta z_c(\rho_i - \rho_w) \tag{14}$$

Finally, we write:

$$\Delta z_c = \frac{P}{g(\rho_i - \rho_w)} \tag{15}$$

Table S1.

References

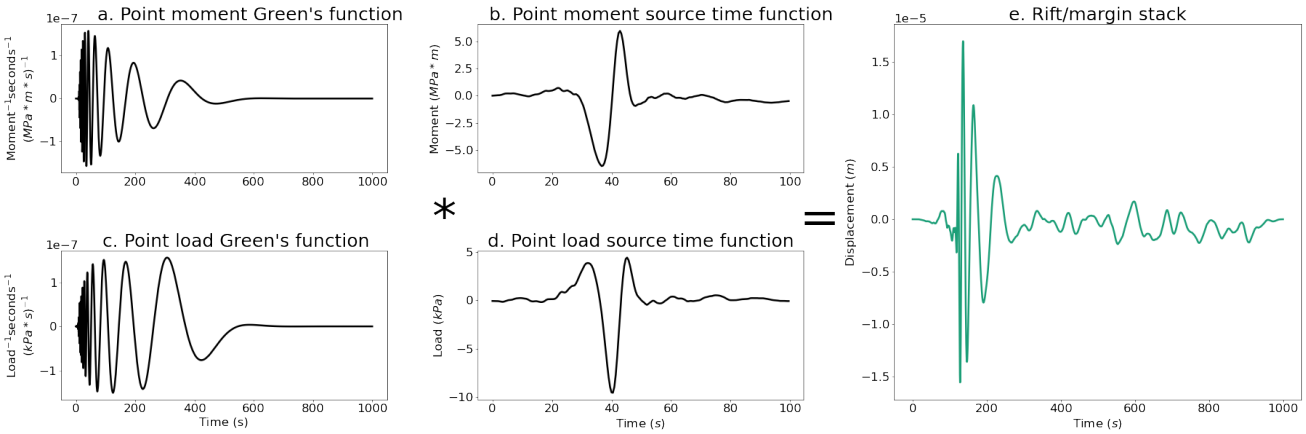

Figure S1. Green's functions and source time functions for rift/margin events. (a) Theoretical Green's function for a bending moment source located at a distance of 30 km, which is approximately the distance from PIG seismic array to the rift/margin area. (b) Source time function retrieved by deconvolving the moment Green's function from the stack of rift/margin vertical displacement waveforms. (c) Theoretical Green's function for a point load source located at a distance of 30 km, which is approximately the distance from PIG seismic array to the rift/margin area. (d) Source time function retrieved by deconvolving the point load Green's function from the stack of rift/margin vertical displacement waveforms. (e) Stack of rift/margin vertical displacement waveforms obtained by aligning waveforms to a master event and taking the mean waveform on the frequency band 0.01-1 Hz.

Table S1. Parameters for building the event catalog.

Parameter	Low Frequency Band	High Frequency Band
STA/LTA band	0.01-1 Hz	1-10 Hz
Short window (ST) length	10 s	10 s
Long window (LT) length	300 s	300 s
Trigger STA/LTA threshold	8 s	20 s
Template matching band	0.05-1 Hz	1-10 Hz
Trigger cross correlation threshold	0.3	0.2
Minimum number of stations for a detection	3	3

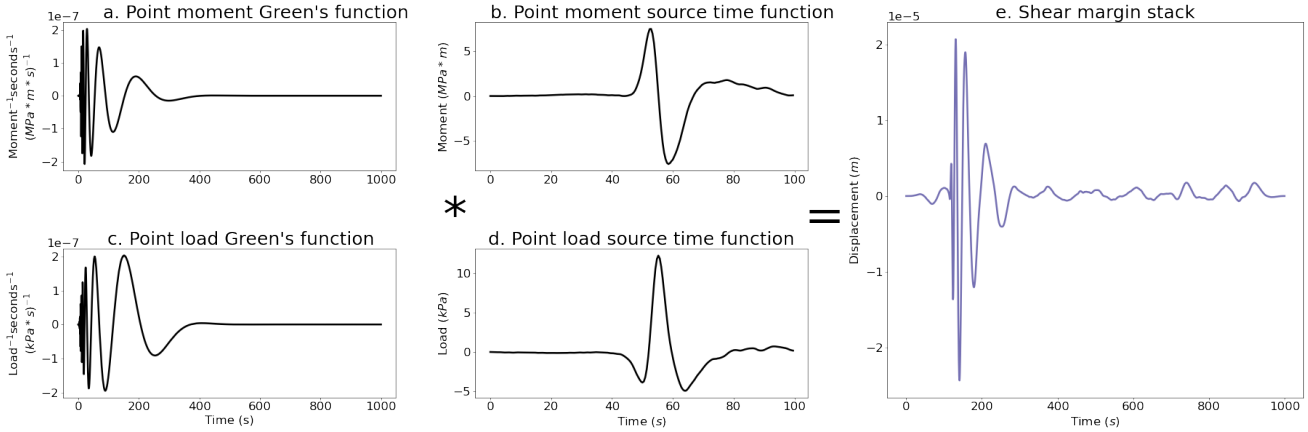

Figure S2. Green's functions and source time functions for shear margin events. (a) Theoretical Green's function for a bending moment source located at a distance of 17.5 km, which is approximately the distance from PIG seismic array to the northeast shear margin near Evans Knoll. (b) Source time function retrieved by deconvolving the moment Green's function from the stack of shear margin vertical displacement waveforms. (c) Theoretical Green's function for a point load source located at a distance of 17.5 km, which is approximately the distance from PIG seismic array to the shear margin. (d) Source time function retrieved by deconvolving the point load Green's function from the stack of shear margin vertical displacement waveforms. (e) Stack of shear margin vertical displacement waveforms obtained by aligning waveforms to a master event and taking the mean waveform on the frequency band 0.01-1 Hz.

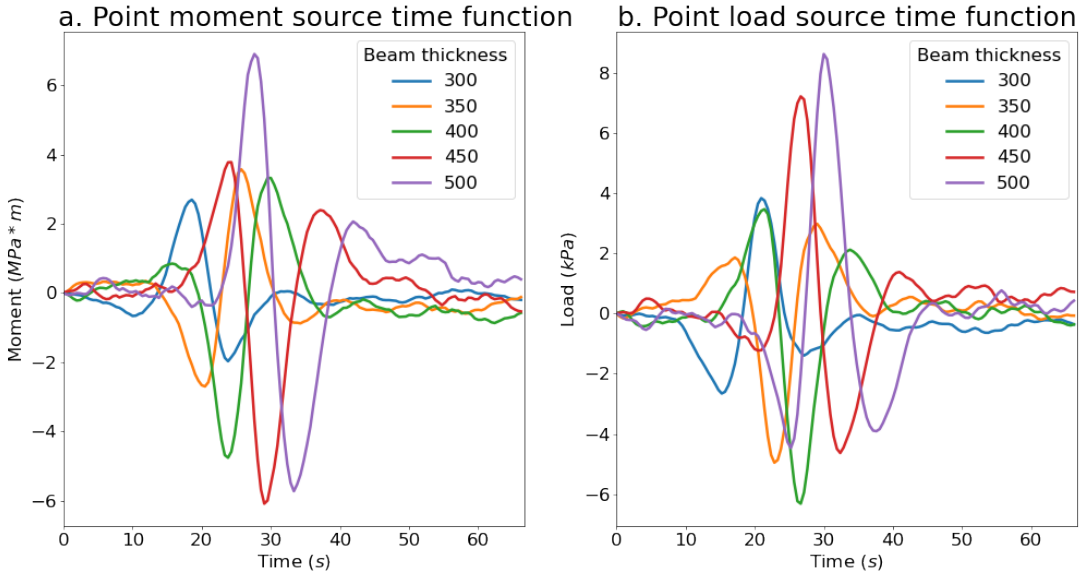

Figure S3. Sensitivity of rift tip source time function deconvolution to modeled ice thickness. Modeled beam thicknesses are shown in the legend. Source time functions generally have larger amplitude and longer duration for thicker beams, because larger forcing is required to induce a given displacement for a more rigid beam. Flexural rigidity, the parameter that governs flexure, is a function of thickness.

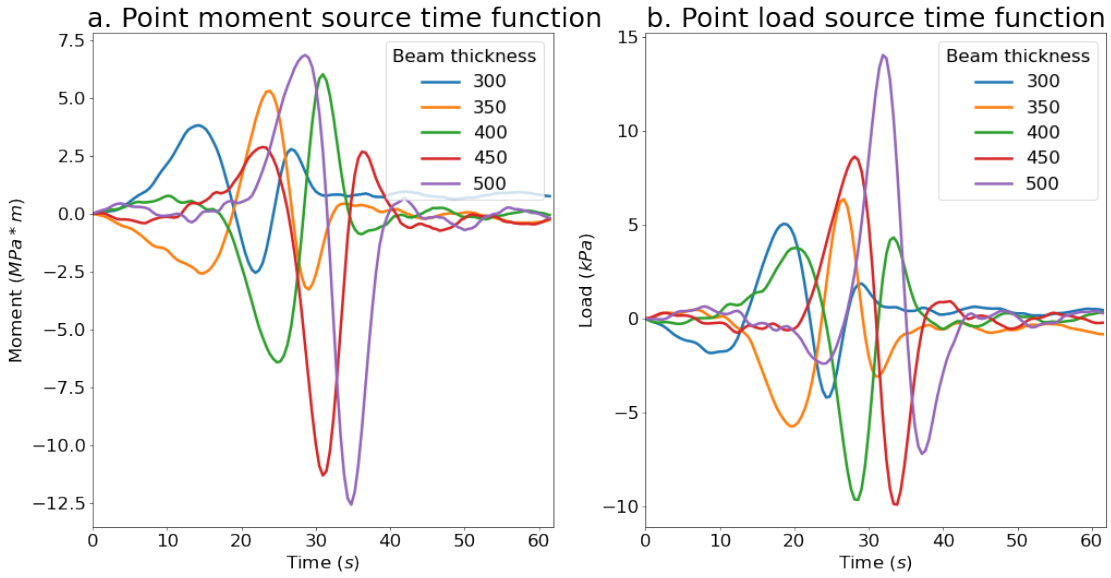

Figure S4. Sensitivity of rift/margin source time function deconvolution to modeled ice thickness. Modeled beam thicknesses are shown in the legend. Source time functions generally have larger amplitude and longer duration for thicker beams, because larger forcing is required to induce a given displacement for a more rigid beam. Flexural rigidity, the parameter that governs flexure, is a function of thickness.

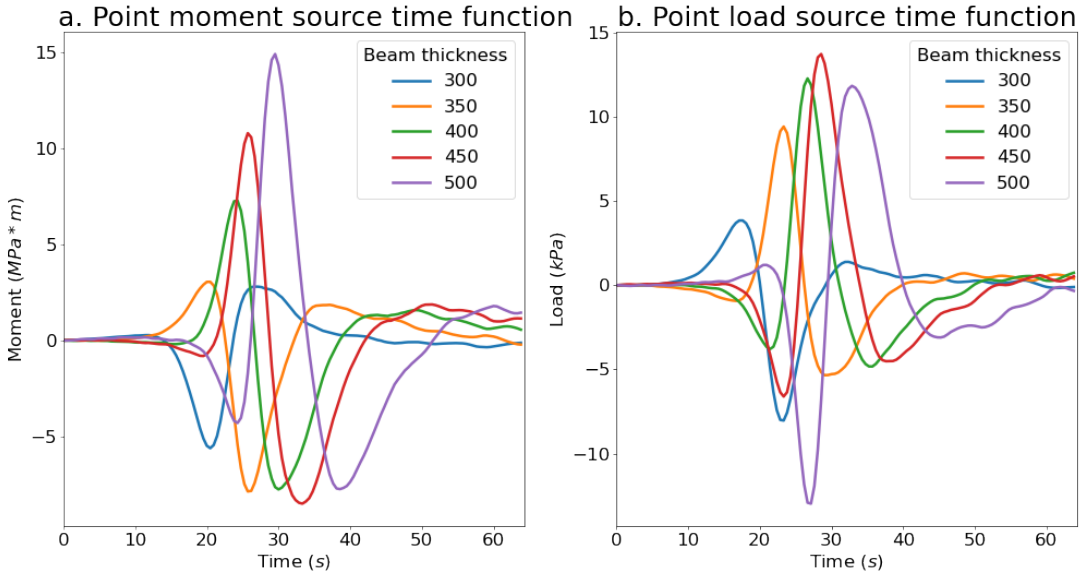

Figure S5. Sensitivity of margin source time function deconvolution to modeled ice thickness. Modeled beam thicknesses are shown in the legend. Source time functions generally have larger amplitude and longer duration for thicker beams, because larger forcing is required to induce a given displacement for a more rigid beam. Flexural rigidity, the parameter that governs flexure, is a function of thickness.

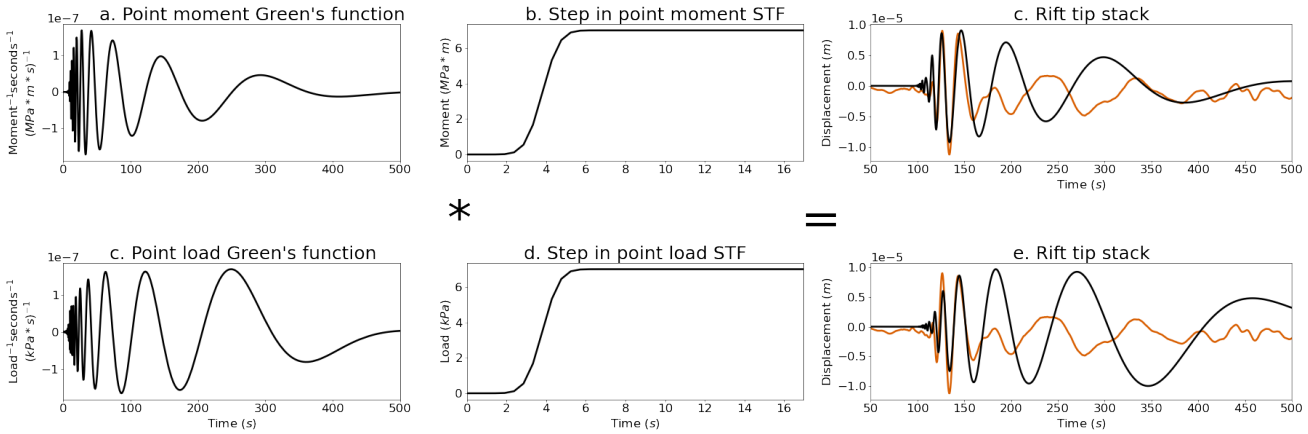

Figure S6. Modeled rift tip Green's function convolved with step source time function. The resulting modeled displacements, shown in black, have a longer decay and larger amplitdue low-frequency displacements than the rift tip stack, shown in orange, for both bending moment and point load sources.

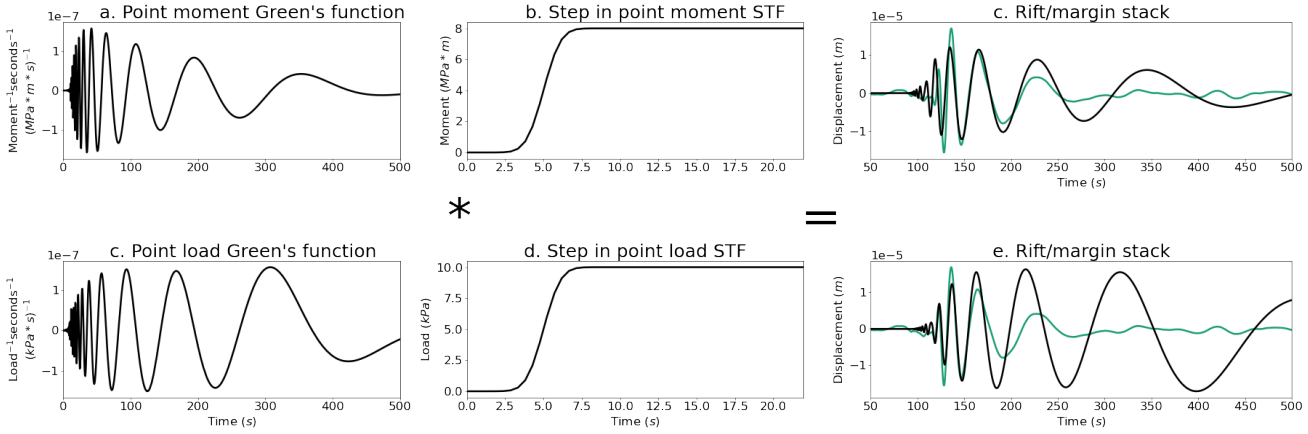

Figure S7. Modeled rift/margin Green's function convolved with step source time function. The resulting modeled displacements, shown in black, have a longer decay and larger amplitdue low-frequency displacements than the rift/margin stack, shown in green, for both bending moment and point load sources.

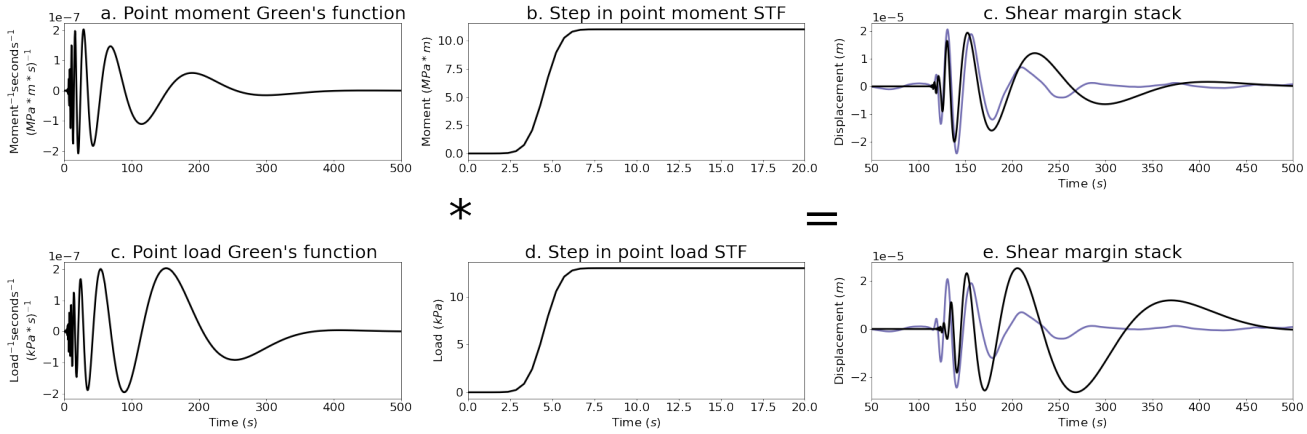

Figure S8. Modeled shear margin Green's function convolved with step source time function. The resulting modeled displacements, shown in black, have a longer decay and larger amplitdue low-frequency displacements than the shear margin stack, shown in purple, for both bending moment and point load sources. The modeled displacements arising from an applied bending moment are relatively similar to the shear margin stack, but the results of deconvolution do not support the hypothesis that the observations were generated by a step forcing in bending moment.

Allen, R. V. (1978, 10). Automatic earthquake recognition and timing from single traces. *Bulletin of the Seismological Society of America*, *68*(5), 1521-1532. Retrieved from https://doi.org/10.1785/BSSA0680051521 doi: 10.1785/BSSA0680051521

Gibbons, S. J., & Ringdal, F. (2006, 04). The detection of low magnitude seismic events using array-based waveform correlation. *Geophysical Journal International*, *165*(1), 149-166. Retrieved from https://doi.org/10.1111/j.1365-246X.2006.02865.x doi: 10.1111/j.1365-246X.2006.02865.x

Paparrizos, J., & Gravano, L. (2016, June). K-shape: Efficient and accurate clustering of time series. *SIGMOD Rec.*, *45*(1), 69–76. Retrieved from https://doi.org/10.1145/2949741.2949758 doi: 10.1145/2949741.2949758